JPhys Energy

PURPOSE-LED PUBLISHING™

PAPER • OPEN ACCESS

Defect engineering in $BiVO_4$ photoanodes: the synergistic role of nitrogen doping and oxygen vacancy for oxygen evolution reaction

To cite this article: Qiuhua Liang *et al* 2025 *J. Phys. Energy* **7** 045030

IOP Publishing J. Phys. Energy 7 (2025) 045030 https://doi.org/10.1088/2515-7655/ae1061

Journal of Physics: Energy

OPEN ACCESS

RECEIVED
21 July 2025

REVISED
23 September 2025

ACCEPTED FOR PUBLICATION
7 October 2025

PUBLISHED
16 October 2025

PAPER

Defect engineering in $BiVO_4$ photoanodes: the synergistic role of nitrogen doping and oxygen vacancy for oxygen evolution reaction

Qiuhua Liang[1,*], **Hassan Ouhbi**[1], **Nicklas Österbacka**[1], **Francesco Ambrosio**[2] and **Julia Wiktor**[1,*]

[1] Department of Physics, Chalmers University of Technology, SE-412 96 Gothenburg, Sweden
[2] Dipartimento di Scienze di Base e Applicate (DiSBA), Universitá degli Studi della Basilicata, Viale dell'Ateneo Lucano, 10-85100 Potenza, Italy
[*] Authors to whom any correspondence should be addressed.

E-mail: qiuhua.liang@chalmers.se and julia.wiktor@chalmers.se

Keywords: density functional theory (DFT), oxygen evolution reaction (OER), photoelectrochemical (PEC) water splitting

Supplementary material for this article is available online

Abstract

Bismuth vanadate ($BiVO_4$) is one of the most promising photoanode materials for water splitting, yet its intrinsic oxygen evolution reaction (OER) performance is limited. Here, we employ hybrid density functional theory calculations to investigate the synergistic effects of nitrogen doping and oxygen vacancy formation on $BiVO_4$ for the OER. We analyze two OER mechanisms, the traditional single-site adsorption evolution mechanism (AEM) and the dual-site bridging mechanism (DSBM), to understand the enhanced catalytic activity observed experimentally. Our results show that nitrogen doping on the surface, combined with the creation of a vanadium active site through oxygen vacancy, significantly reduces the OER overpotential from 1.44 V in pristine $BiVO_4$ to 0.93 V (AEM) and 1.16 V (DSBM). Besides, the nitrogen dopants on the surface alter the local acid-base chemistry: proton adsorption on nitrogen becomes 0.52 eV more favorable than on oxygen, and water dissociation is 0.31 eV easier at the V site than at the Bi site. By offering low-energy proton-binding sites, nitrogen stabilizes key intermediates and favors formation of a stable O–O dimer, producing a pronounced reduction in overpotential. These findings highlight that the effective defect engineering strategies can significantly enhance the overall performance of $BiVO_4$-based photoanodes in operational photoelectrochemical systems.

1. Introduction

Photoelectrochemical (PEC) water splitting is a promising approach for hydrogen production by converting water and sunlight into storable chemical energy without producing harmful by-products [1–3]. In PEC water splitting, the hydrogen evolution reaction occurs at the cathode, while the oxygen evolution reaction (OER) takes place at the anode [4]. The latter reaction involves a complex four-electron transfer process with high-energy intermediates, making it the primary bottleneck due to its sluggish kinetics and high overpotentials [5]. Nowadays, significant research efforts have thus focused on developing semiconductor-based photoanodes capable of efficiently catalyzing the OER under solar illumination [6–8]. Among various candidate materials, bismuth vanadate ($BiVO_4$) has emerged as one of the most promising oxide photoanodes, owing to its moderate band gap ~2.4 eV for visible light absorption, low cost, ease of synthesis [9], robust stability against PEC and chemical corrosion [9, 10], and favorable valence band edge alignment for water oxidation reaction [11]. Despite these advantages, the practical PEC performance of pristine $BiVO_4$ remains hindered by several limitations. First, its charge carrier mobility is relatively low [12], constraining large-scale photocatalytic applications. Second, although $BiVO_4$ can harvest a substantial portion of visible light, further extension of adsorption into longer wavelengths is highly desirable to maximize solar photon utilization [13]. Third, rapid recombination of photogenerated electron–hole pairs reduces the efficiency of interfacial charge transfer [14, 15].

Addressing these challenges has spurred diverse engineering strategies aimed at enhancing both bulk and interfacial properties of $BiVO_4$, thereby improving its PEC performance.

To address these limitations, various strategies have been explored, such as morphological engineering [16, 17], doping with foreign elements [18–20], introducing surface vacancies [21–23], and creating heterojunctions [24–26]. For example, Wang *et al* [23] reported that the oxygen vacancies can increase the electron carrier concentration in $BiVO_4$. Hu *et al* [21] found that introducing oxygen vacancies on surface converts previously inactivate V sites into catalytic centers, thereby expanding the number of available active sites. Moreover, Seo *et al* [27] found that N atoms can be introduced into $BiVO_4$ by substituting oxygen atoms, the co-doping $BiVO_4$ with nitrogen and oxygen vacancies can substantially improve both carrier concentration and mobility by promoting polaron formation and reducing polaron formation energy. Similarly, Österbacka *et al* [28] showed that surface oxygen vacancies in $BiVO_4$ spontaneously ionize, and these ionized vacancies makes the OER more thermodynamically favorable while enhancing the carrier concentration.

A key experimental investigation demonstrated that annealing nanoporous $BiVO_4$ in a mild N_2 atmosphere at ∼350 °C effectively incorporates nitrogen into the lattice and induces the formation of oxygen vacancies [29]. In addition to facilitating oxygen vacancy formation, this treatment narrows the band gap by ∼0.2 eV by introducing states within the gap, improves charge separation, and increases solar photon absorption, leading to water-splitting efficiencies exceeding 2% [29]. Despite these promising findings, the precise atomic-level mechanisms by which nitrogen doping and oxygen vacancy synergistically enhance OER performance remain insufficiently understood. Consequently, density functional theory (DFT) calculations are essential for systematically examining how nitrogen doping and associated oxygen defects modify the water oxidation activity of $BiVO_4$, thereby elucidating the reaction pathways responsible for improved OER efficiency in nitrogen-doped $BiVO_4$.

In this work, we use hybrid DFT calculations to investigate how nitrogen incorporation alters the catalytic landscape of $BiVO_4$. Charge-neutral doping is achieved by replacing three oxygens (oxidation state −2) with two nitrogen atoms (oxidation state −3) either in the surface (outermost layer) or subsurface (one layer below). Two reaction pathways are analyzed: (i) the conventional single-site adsorption-evolution mechanism (AEM), where *OH, *O, and *OOH adsorb and react at a single Bi or V site, and (ii) a dual-site bridging mechanism (DSBM), in which neighboring Bi and V work cooperatively to stabilize intermediates and facilitate O–O bond formation across both sites. The calculations reveal that surface doping lowers the AEM overpotential to 0.93 V (versus 1.44 V for pristine $BiVO_4$) and the DSBM overpotential to 1.16 V, whereas an equivalent subsurface doping offers little or no benefit. Additionally, the surface doping stabilizes a superoxide-like O_2^{1-} dimer, while subsurface doping favors a less reactive peroxide-like O_2^{2-}, explaining the divergent catalytic activities. Nitrogen also alters the local acid-base chemistry: proton adsorption is ∼0.5 eV stronger on N than on O, and water dissociation is ∼0.3 eV easier at a V site than at Bi, further lowering the kinetic barrier. These atomistic insights highlight the dual structural-and-chemical role of surface nitrogen doping with its adjacent oxygen vacancy and provide design rules for defect-engineered $BiVO_4$ photo-anodes.

2. Computational details and OER theory

2.1. Computational details

All calculations presented in this study are performed using hybrid DFT within the Gaussian plane-waves method, as implemented in the CP2K package [30]. Goedecker–Teter–Hutter pseudopotentials are used to describe the core-valence interactions [31]. Gaussian-type DZVP-MOLOPT basis sets are employed [32], and a plane-wave energy cutoff of 600 Ry is set to expand the electron density and REL_CUTOFF = 80 Ry. Exchange–correlation interactions are described using the hybrid PBE0 functional with a fraction of exact exchange set to 0.22 [11]. The fundamental bandgap produced by this parameter is consistent with the bandgap calculated by QSG $\tilde{W}$ method [33, 34]. This parameter also gives a bandgap in good agreement with experiments, once additional effects are considered [35]. An auxiliary density matrix method with a cFIT auxiliary basis set is employed to reduce computational costs associated with the hybrid functional calculations. Geometry optimization is carried out until the maximum residual force on atoms fell below 1.94×10^{-4} Hartree Bohr^{-1}. The Brillouin zone is sampled at the Γ point. We consider the (001) surface of $I4_1/a$ tetragonal scheelite $BiVO_4$, whose electronic properties are near identical to those of the monoclinic phase, constructed using a $2\times2\times2$ repetition of the primitive structure ($a = b = 5.147$ Å, $c = 11.726$ Å) [28]. This model consists of eight layers containing 192 atoms and 30 Å of vacuum in the surface normal direction are used, ensuring sufficient vacuum spacing to prevent interactions between periodic images; thus Γ point is sufficient for this size. SCF used OT minimization. Spin-polarized calculations are performed to account for the presence of unpaired electrons.

2.2. OER theory

In this study, we consider two possible pathways for the OER under acidic conditions: the traditional AEM [36, 37], which proceeds at a single active site; and the DSBM [38–40], which involves two neighboring active sites. The overall water oxidation reaction is:

$$2H_2O\,(l) \rightarrow O_2 + 4H^+ + 4e^-,\ \Delta G_0 = 4.92\,\mathrm{eV} \tag{1}$$

where (l) refers to the liquid phase, and $\Delta G_0 = 4.92\,\mathrm{eV}$ is the experimentally measured Gibbs free energy for this reaction.

Under the AEM pathway, the OER is usually assumed consisting of four steps, each involving a proton–electron transfer:

$$H_2O\,(l) + *\ \rightarrow {}^*\mathrm{OH} + H^+ + e^-, \tag{2}$$

$$^*\mathrm{OH} \rightarrow {}^* \mathrm{O} + H^+ + e^-, \tag{3}$$

$$H_2O\,(l) + {}^*\mathrm{O} \rightarrow {}^*\mathrm{OOH} + H^+ + e^-, \tag{4}$$

$$^*\mathrm{OOH} \rightarrow * + O_2\,(g) + H^+ + e^-, \tag{5}$$

where $*$ represents the catalyst's active site (either a Bi site or a V site exposed on the surface as a consequence of the formation of the oxygen vacancy). The intermediate species *OH, *O, and *OOH refer to the respective adsorbates bound to the active site. We employ the computational hydrogen electrode (CHE) approach, which assumes equilibrium in the reaction $H^+ + e^- \leftrightarrow 1/2\ H_2$ at $T = 298\,\mathrm{K}$ and $p_{H_2} = 1\,\mathrm{bar}$, along with equilibrium between liquid and gaseous water $H_2O(l) \leftrightarrow H_2O(g)$ at $T = 298\,\mathrm{K}$ and $p_{H_2O} = 0.035\,\mathrm{bar}$ [41]. In this model, explicit liquid water is not included. This approach has been widely used to evaluate OER thermodynamics on lots of systems without explicit solvation [36, 41]. The omission of solvent means that polar intermediates such as *OH and *OOH may be somewhat overestimated in energy; however, solvent stabilization tends to shift both reactants and products similarly, and thus relative trends and the potential-determining step (PDS) are expected to be preserved [42]. Our main conclusions, which focus on the thermodynamic effect of surface modification on OER energetics, are therefore robust. The Gibbs free energy changes for reactions (2)–(5) are given by:

$$\Delta G_1 = E({}^*\mathrm{OH}) - E(*) - E_{H_2O} + \tfrac{1}{2}E_{H_2} + (\Delta \mathrm{ZPE} - T\Delta S)_1\,, \tag{6}$$

$$\Delta G_2 = E({}^*\mathrm{O}) - E({}^*\mathrm{OH}) + \tfrac{1}{2}E_{H_2} + (\Delta \mathrm{ZPE} - T\Delta S)_2\,, \tag{7}$$

$$\Delta G_3 = E({}^*\mathrm{OOH}) - E({}^*\mathrm{O}) - E_{H_2O} + \tfrac{1}{2}E_{H_2} + (\Delta \mathrm{ZPE} - T\Delta S)_3\,, \tag{8}$$

$$\Delta G_4 = \Delta G_0 - (\Delta G_1 + \Delta G_2 + \Delta G_3)\,. \tag{9}$$

Here, $E(*)$, $E(^*\mathrm{OH})$, $E(^*\mathrm{O})$, and $E(^*\mathrm{OOH})$ are the hybrid DFT-calculated total energies of the clean surface and surfaces with the respective adsorbates; E_{H_2O} and E_{H_2} are the hybrid DFT-calculated total energies of isolated H_2O and H_2 molecules. ΔZPE and $T\Delta S$ are the changes in vibrational zero-point energies and entropy contributions, respectively, at temperature T. All Energies were obtained without an empirical dispersion term. For ionic oxide surfaces with strongly chemisorbed OER intermediates (*OH, *O, *OOH), the dominant bonding is ionic; literature benchmarks indicate that semi-empirical dispersion terms (D3/Tkatchenko–Scheffler van der Waals correction) mainly affect physisorbed/weakly bound adsorbates, while having much smaller effect on chemisorption reaction steps [43, 44]. Accurately treating gas-phase O_2 in DFT-even with hybrid functionals remains non-trivial: the triplet ground state is reproduced, but the computed reaction energy typically deviates from the experimental value (4.92 eV) by $\sim$0.04–0.10 eV in our tests (PBE0 gives $\approx$ 4.82–4.98 eV for our basis/cut-off). To avoid propagating this small but systematic error into the last OER step, we follow the common CHE approach and obtain ΔG_4 by subtracting the first three steps from the experimental overall free energy (4.92 eV). This procedure removes the residual O_2 energy bias while retaining the accuracy benefits of using the hybrid functional.

According to previous studies [38–40], the DSBM is another viable OER pathway that becomes relevant when two neighboring active sites are present on the surface. Like the AEM mechanism, the DSBM also involves four proton–electron transfer steps. However, its distinguishing feature lies in the last three steps: once *OH is formed on one active site, a second *OH can absorb on the other adjacent active site (the second step), ultimately generating coexisting *O and *OH intermediates on dual active sites (the third step). The final release of O_2 proceeds from these *O and *OH intermediates on dual active sites (the fourth step). In our case, the Bi site and V site (with an oxygen vacancy) serve as potential active sites, denoted *(Bi) and *(V), respectively. The overall DSBM pathway can be written as:

$$H_2O\,(l) + \left(*_{(V)} + *_{(Bi)}\right) \rightarrow \left(*_{(V)}OH + *_{(Bi)}\right) + H^+ + e^-\,, \tag{10}$$

$$H_2O\,(l) + \left(*_{(V)}OH + *_{(Bi)}\right) \rightarrow \left(*_{(V)}OH + *_{(Bi)}OH\right) + H^+ + e^-\,, \tag{11}$$

$$\left(*_{(V)}OH + *_{(Bi)}OH\right) \rightarrow \left(*_{(V)}O + *_{(Bi)}OH\right) + H^+ + e^-\,, \tag{12}$$

$$\left(*_{(V)}O + *_{(Bi)}OH\right) \rightarrow \left(*_{(V)} + *_{(Bi)}\right) + O_2\,(g) + H^+ + e^-\,. \tag{13}$$

The Gibbs free energy of reactions (10)–(13) are then given by:

$$\Delta G_1 = E(*_{(V)}OH + *_{(Bi))}) - E(*_{(V)} + *_{(Bi)}) - E_{H_2O} + \tfrac{1}{2}E_{H_2} + (\Delta ZPE - T\Delta S)_1\,, \tag{14}$$

$$\Delta G_2 = E\left(*_{(V)}OH + *_{(Bi)}OH\right) - E\left(*_{(V)}OH + *_{(Bi)}\right) - E_{H_2O} + \tfrac{1}{2}E_{H_2} + (\Delta ZPE - T\Delta S)_2\,, \tag{15}$$

$$\Delta G_3 = E\left(*_{(V)}O + *_{(Bi)}OH\right) - E\left(*_{(V)}OH + *_{(Bi)}OH\right) + \tfrac{1}{2}E_{H_2} + (\Delta ZPE - T\Delta S)_3\,, \tag{16}$$

$$\Delta G_4 = \Delta G_0 - (\Delta G_1 + \Delta G_2 + \Delta G_3)\,. \tag{17}$$

For an ideal catalyst, the total Gibbs free energy ΔG_0 (4.92 eV) would be evenly distributed among these four steps, yielding $\Delta G_0/4 = 1.23$ eV per step. In practice, however, the free energy varies, resulting in an overpotential that corresponds to the step with the largest free energy requirement. The overpotential is given by:

$$\eta = \frac{\Delta G_{max} - 1.23}{e}, \tag{18}$$

where ΔG_{max} is the largest of the four reaction energies and e is the elementary charge.

3. Results and discussion

Extensive literature demonstrates the feasibility and stability of N substitute doping and oxygen vacancies in $BiVO_4$, both experimentally and theoretically [27–29]. Here, we consider a range of N-doped $BiVO_4$ models and retained only the lowest-energy surface and subsurface configurations for OER calculations. A previous study has found that substitutional N is more stable than interstitial in $BiVO_4$ [27]. Therefore, in each case, two neighboring oxygen atoms at adjacent Bi sites are replaced by two nitrogen atoms. The corresponding defect formation energies and *ab initio* molecular dynamics (AIMD) simulation have been performed to test the thermodynamic stability of the most stable configurations (see the supporting information for more details). For surface doping, the N dopants lie at the outermost layer, and the associated oxygen vacancy stabilizes at the outermost layer and is coordinated to adjacent V and Bi atoms that do not bond to nitrogen. For subsurface doping, the N dopants are one layer below the surface, and the vacancy is preferentially positioned within the layer below the surface as well. In this configuration, the oxygen vacancy is located between a V atom bonded to nitrogen and a Bi atom that is not. Following the nitrogen doping and creation of an oxygen vacancy, both Bi and V sites can serve as active sites. We evaluated the stable OER intermediates (OH, O, and OOH) under the AEM pathway [reactions (2)–(5)] on both N-$BiVO_4$ surface and subsurface, focusing on four active site configurations: S-*Bi, S-*V, Sub-*Bi, and Sub-*V. The corresponding active site is indicated by an arrow in figure 1. Here, 'S-' denotes models in which the N dopants lie in the outermost layer, while 'Sub-' indicates that they are one layer below. The symbol following the asterisk (*Bi or *V) identifies the metal atom that

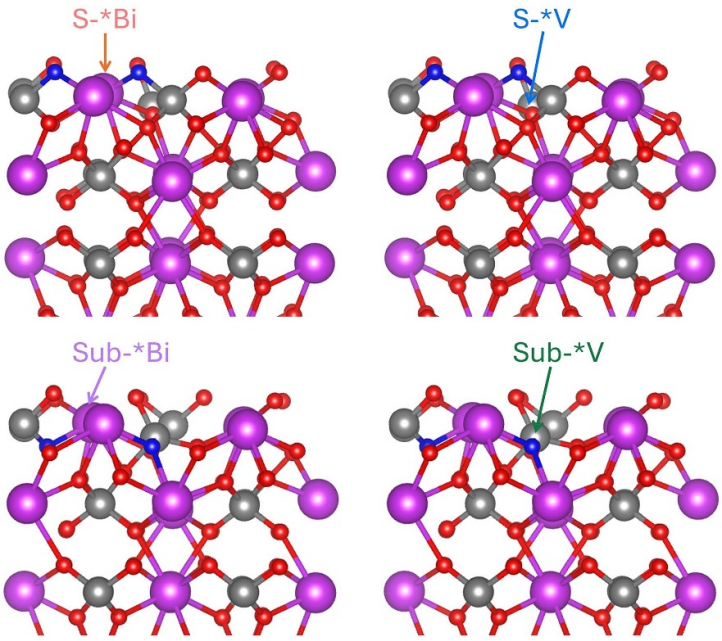

Figure 1. Side view of N-$BiVO_4$ surface and subsurface in configurations S-*Bi, S-*V, Sub-*Bi, and Sub-*V. The corresponding active site is indicated by arrow. The purple, gray, red, and blue spheres represent Bi, V, O and N atoms, respectively.

directly binds the OER intermediates. Thus, *Bi in S-*Bi and Sub-*Bi refers to crystallographically equivalent Bi sites that differ only in N dopants depth. Specifically, S-*Bi denotes surface nitrogen doping with Bi as the active site, S-*V denotes surface nitrogen doping with V as the active site. In the subsurface cases, Sub-*Bi denotes subsurface nitrogen doping with Bi as the active site, and Sub-*V denotes subsurface nitrogen doping with V as the active site.

For the AEM mechanism, the OH, O and OOH intermediates adsorb at the top of the active site. This conventional adsorption sequence is observed for both S-*Bi and Sub-*Bi systems (figure 2). The S-*V and Sub-*V systems follow the same pattern for the first two steps: the OH and O adsorb on the V site. The third step, however, diverges. Previous studies have indicated that when the V site contains an oxygen vacancy, an O–O dimer formation becomes energetically favorable [28, 45]. Accordingly, in our S-*V configuration, we consider not only standard OOH adsorption but also H desorption from OOH and subsequent O–O bond formation on the active site. We define three configurations to explore these possibilities (figure 3). In S-*V(OOH1), the OOH intermediate adsorbs intact on a single active site without proton desorption. In S-*V(OOH2), an O–O dimer forms at the V with the dissociated H adsorbing on a nearby oxygen atom. Since N-doping may make it easier for the OOH to donate protons, we introduce S-*V(OOH3), in which the O–O dimer is adsorbed at the V site while the H binds to a nitrogen atom on the surface.

Taking S-*V(OOH1) as reference, S-*V(OOH2) and S-*V(OOH3) are 0.32 eV and 0.88 eV lower in energy, respectively, indicating that S-*V(OOH3) is the most stable configuration. In this configuration the O–O dimer bond length is 1.32 Å. We also calculate the density derived electrostatic and chemical (DDEC6) charge using the Chargemol code [46] and find a value of −0.58 e. Hydrogen preferentially adsorbs on the nitrogen site rather than on the oxygen site. Thus, when a V site adjacent to an oxygen vacancy acts as the active site, proton desorption from the *OOH intermediate is thermodynamically favored, and the resulting O–O dimer is stabilized on the V atom with the proton anchored to nitrogen. The nitrogen dopant therefore provides a low-energy hydrogen-binding site that further stabilizes the O–O dimer.

Furthermore, in the Sub-*V configuration, beyond conventional OOH adsorption, the formation of an O–O dimer with H desorption is also possible. To investigate this, we consider three scenarios as shown in figure 4: in Sub-*V(OOH1), the OOH intermediate remains bound to a single V site, representing the conventional adsorption configuration; in Sub-*V(OOH2), an O–O dimer forms at the V site, and the desorbed hydrogen adsorbs on a nearby surface oxygen that bonds to both Bi and V atoms, without nitrogen substitution; in Sub-*V(OOH3), the O–O dimer also adsorbs on the V site with an O–O bond length of 1.44 Å and carries charge −0.95 e, while the hydrogen binds to a neighboring oxygen atom that is likewise coordinated to both Bi and V. Using Sub-*V(OOH1) as the reference configuration

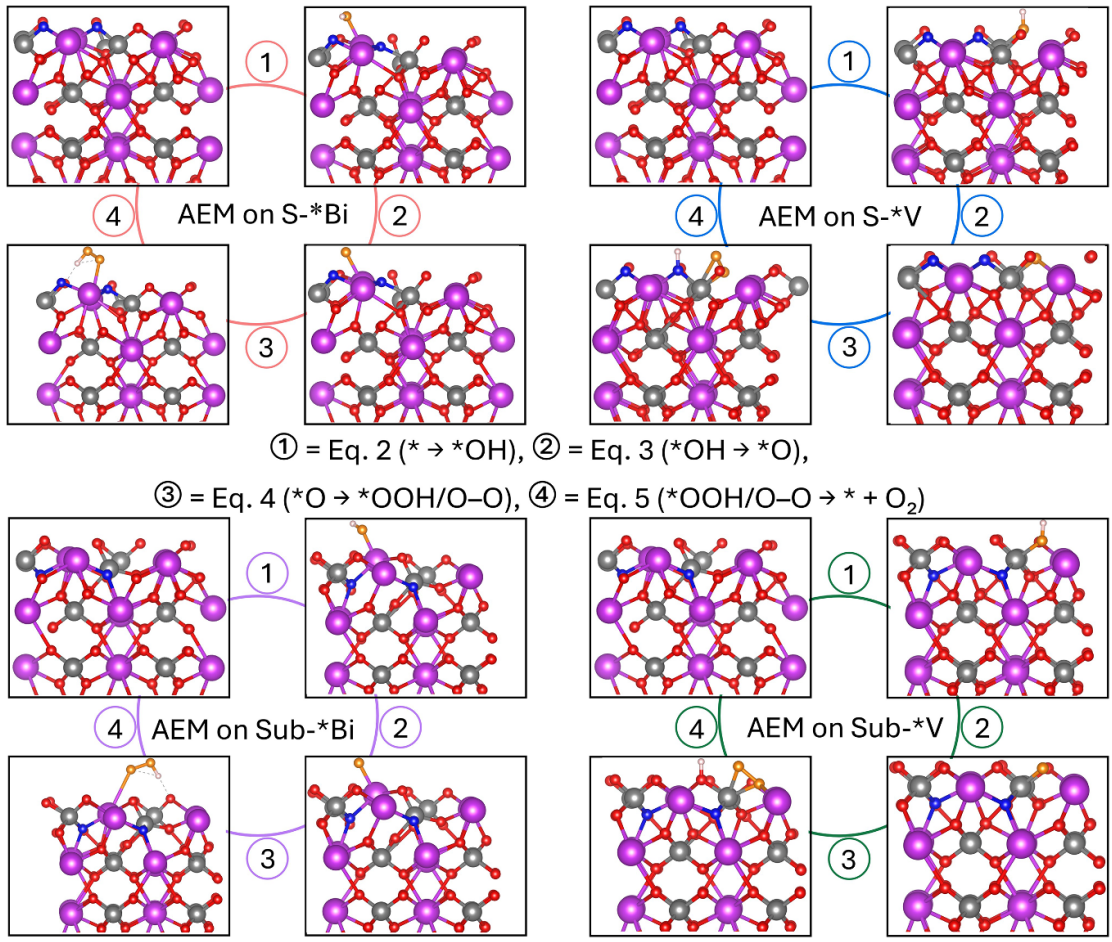

Figure 2. Side view of the AEM reaction cycle, reactions (2)–(5), for S-*Bi, S-*V, Sub-*Bi, and Sub-*V, respectively. The intermediate species O and H atoms are marked by yellow and white spheres, with dashed lines indicating hydrogen bonds.

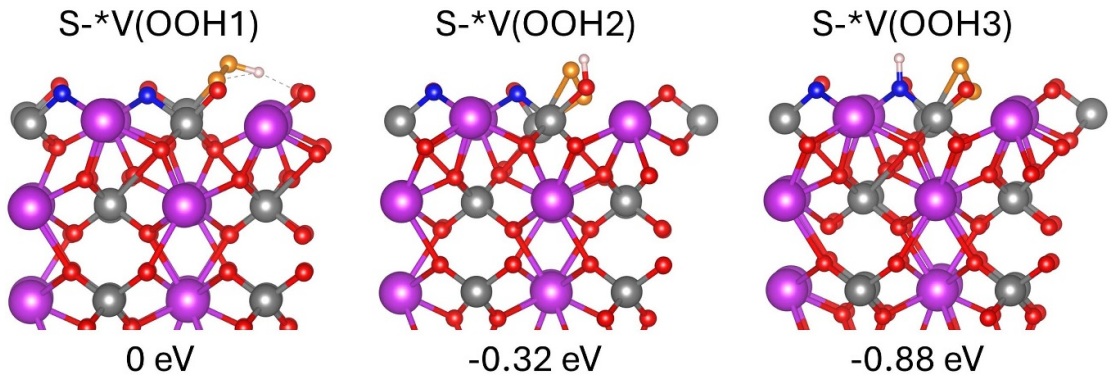

Figure 3. Side view of OOH adsorption and O–O dimer formation at the S-*V site in three different configurations. In S-*V(OOH1), the OOH intermediate adsorbs on a single V site and is used as the reference configuration with its energy set to 0 eV. In S-*V(OOH2) and S-*V(OOH3), O–O dimer formation occurs with proton desorption, where the proton adsorbs on an oxygen and nitrogen site, respectively.

(0 eV), Sub-*V(OOH2) is 0.21 eV higher in energy, whereas Sub-*V(OOH3) is 0.16 eV lower, indicating that Sub-*V(OOH3) is the most stable of the three. Therefore, Sub-*V(OOH3) is used as the representative intermediate in the third step of the AEM pathway for this configuration.

The corresponding free energy profiles (equations (6)–(9)) for each step are shown in figure 5, with the PDS indicated by a solid line between the two relevant reaction steps. The overall Gibbs free energy difference between the initial state, marked *, and the final state, marked * + O_2, is fixed at 4.92 eV. The free energy profile of pristine $BiVO_4$ is included to enable direct comparisons of overpotentials (η) between configurations. For pristine $BiVO_4$, the surface Bi site serves as the primary active site, and our

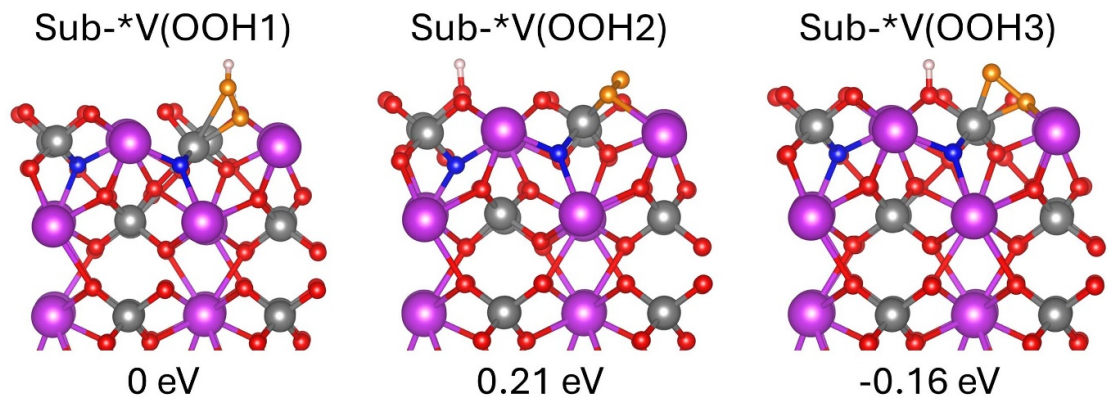

Figure 4. Side view of OOH adsorption and O–O dimer formation at the Sub-*V site in three different configurations. Sub-*V(OOH1), where the OOH intermediate is adsorbed on a single V site, serves as the reference configuration with its energy set to 0 eV. In Sub-*V(OOH2) and Sub-*V(OOH3), O–O dimer formation occurs with proton desorption, where the hydrogen adsorbs on neighboring oxygen atoms with different bonding environments.

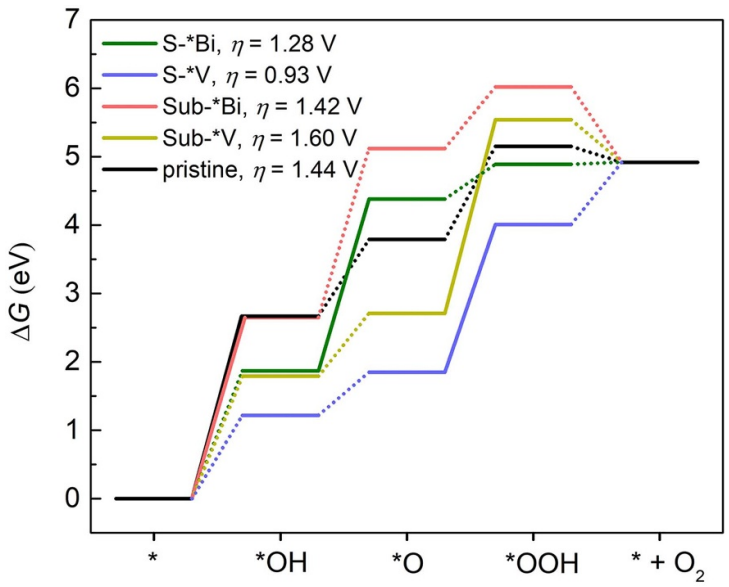

Figure 5. Gibbs free energy profiles of N-$BiVO_4$ surface and subsurface with *Bi and *V as active site, respectively. The PDS is indicated by the solid line between the two relevant reaction steps.

calculations yield an η of 1.44 V, with the PDS identified as the formation of *OH. This value aligns closely with a previously reported result of 1.40 V [28], corroborating the reliability of our computational approach. Additional details on the OER reaction on pristine $BiVO_4$ can be found in [28].

Doping noticeably affects the OER performance. In the S-*Bi configuration, the η decreases to 1.28 V, with the PDS shifting from *OH to *O. Notably, S-*V configuration reduces η even further to 0.93 V, shifting the PDS to *OOH formation. Conversely, Sub-*Bi configuration offers only a modest improvement ($\eta = 1.42$ V), maintaining the same PDS as pristine $BiVO_4$, whereas Sub-*V increases η to 1.60 V with the PDS involving the *OOH formation. These results indicate that nitrogen doping at the surface (especially activating the V site) substantially modifies the adsorption of OER intermediates and strongly enhances catalytic activity. Meanwhile, doping at the subsurface shows limited benefits at the Bi site and may adversely affect performance at the V site. Therefore, both the formation of O–O dimer and direct involvement of surface nitrogen contribute to lowering the OER overpotential, underscoring the critical role of strategic defect engineering in optimizing $BiVO_4$ OER catalyst performance.

To interpret the overpotential trend, we evaluate the Gibbs free energies of adsorption ΔG_{ADS}, where ADS is the adsorbed species *OH, *O, or *OOH, using [6, 47]:

$$\Delta G(^*\mathrm{OH}) = \Delta G_1 = E(^*\mathrm{OH}) - E(^*) - E_{\mathrm{H_2O}} + \tfrac{1}{2}E_{\mathrm{H_2}} + (\Delta \mathrm{ZPE} - T\Delta S)_1 \,, \tag{19}$$

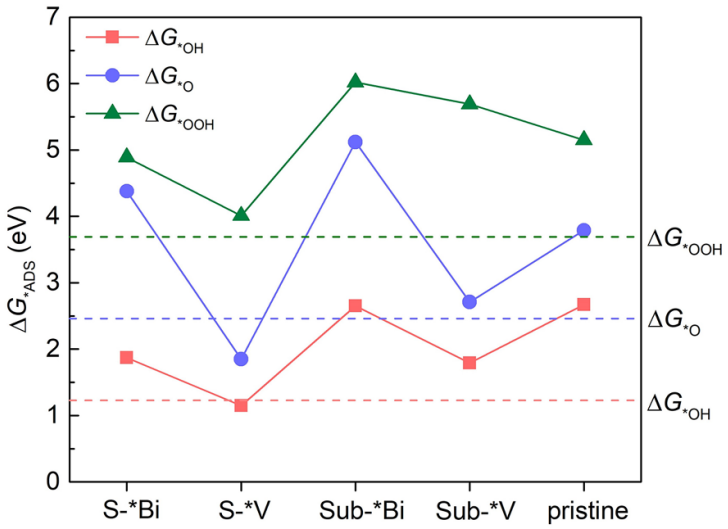

Figure 6. Gibbs free energies of the OER intermediates on S-*Bi, S-*V, Sub-*Bi, Sub-*V, and pristine $BiVO_4$. Adsorbed species are abbreviated as ADS and correspond to *OH (pink squares), *O (blue circles), and *OOH (green triangles). The dashed horizontal lines at 1.23 eV (pink), 2.46 eV (blue), and 3.69 eV (green) mark the ideal free energies for *OH, *O, and *OOH, respectively.

$$\Delta G(^*\mathrm{O}) = \Delta G_1 + \Delta G_2 = E(^*\mathrm{O}) - E(^*) - E_{\mathrm{H_2O}} + E_{\mathrm{H_2}} + (\Delta \mathrm{ZPE} - T\Delta S)_{1+2}\,, \tag{20}$$

$$\Delta G(^*\mathrm{OOH}) = \Delta G_1 + \Delta G_2 + \Delta G_3 = E(^*\mathrm{OOH}) - E(^*) - 2E_{\mathrm{H_2O}} + \tfrac{3}{2}E_{\mathrm{H_2}} + (\Delta \mathrm{ZPE} - T\Delta S)_{1+2+3}\,. \tag{21}$$

The resulting values are plotted in figure 6. As a comparison, the ideal Gibbs free energies for $\Delta G(^*\mathrm{OH})$, $\Delta G(^*\mathrm{O})$, and $\Delta G(^*\mathrm{OOH})$ are also shown. The total free energy for water oxidation is 4.92 eV, so an ideal catalyst would distribute this evenly across the four proton–electron steps (4.92 eV/4 = 1.23 eV per step). Accordingly, the ideal adsorption free energies are 1.23 eV for $\Delta G(^*\mathrm{OH})$, 2.46 eV for $\Delta G(^*\mathrm{O})$, and 3.69 eV for $\Delta G(^*\mathrm{OOH})$, as shown by the horizontal dashed lines in figure 6. The higher the free energy than the ideal values, the weaker the bonding of the intermediate to the active site.

On pristine $BiVO_4$, all values lie well above the ideal values, with OH binding being particularly weak ($\Delta G(^*\mathrm{OH}) \approx 2.7$ eV), which makes *OH formation the PDS and produces the high η of 1.44 V. For S-*Bi, nitrogen strengthens OH bonding but simultaneously weakens O bonding, shifting the PDS to *O formation; the net effect is a modest reduction of η to 1.28 V. For the S-*V, $\Delta G(^*\mathrm{OH})$ decreases to essentially the ideal value, while $\Delta G(^*\mathrm{O})$ moves slightly below and $\Delta G(^*\mathrm{OOH})$ slightly above the ideal line. This near-balanced stabilization of all three intermediate shifts the PDS to the *OOH formation, and yields the lowest η of 0.93 V. The Sub-*Bi energies nearly coincide with those of pristine $BiVO_4$, explaining the minor drop in η to 1.42 V. On Sub-*V, although $\Delta G(^*\mathrm{OH})$ and $\Delta G(^*\mathrm{O})$ move closer to ideal values, $\Delta G(^*\mathrm{OOH})$ increases sharply, leaving *OOH far too weakly bound. The large gap between *O and *OOH becomes the new PDS, raising the η to 1.60 V. Therefore, the overpotential trend mirrors how closely each set of adsorption energies approaches the ideal 1.23 eV spacing, with the S-*V providing the most favorable balance, followed by S-*Bi, whereas both subsurface models offer little or no catalytic benefit.

To clarify why the overpotential drops for the N-doped surface, we quantify DDEC6 charge of the nitrogen dopants and all OER intermediates (table S2). On pristine $BiVO_4$ ($\eta = 1.44$ V) the intermediates retain radical or singly reduced character in the form of OH radical (+0.03 e), O^- species (−0.50 e), and OOH radical (+0.04 e). In the clean N-$BiVO_4$ slabs the two nitrogen dopants are close to an N^{3-} oxidation state (~ -1.1 e on the surface, −1.3 e in the subsurface). On the surface and subsurface Bi systems, adsorption of OH and O draws ∼0.3–0.4 e from the N nearest the active site, forming N^{2-} (N ≈ −0.87 e surface, −0.90 e subsurface) and stabilizing highly reduced OH^-/O^- fragments (∼ -0.40 e each). Nitrogen returns to N^{3-} upon *OOH adsorption. The extra electron donation to $^*OH^-/O^-$ (−0.40 e vs +0.03 e in pristine $BiVO_4$) explains the modest overpotential drop at Bi sites ($\eta = 1.28$ for surface doping and 1.42 V for subsurface doping). When intermediates adsorb at surface or subsurface V site, nitrogen donates even more charge: from N^{2-}/N^{3-} for OH adsorption to N^{2-}/N^{2-} for O adsorption,

Table 1. Calculated values (eV) of $\Delta_{ads}H^+$, $\Delta_{ads}H_2O$, $\Delta_{ads}OH^-$ (equations (26)–(28)).

Δ_{ads}	Energy (eV)
H^+	+0.52
H_2O	−0.08
OH^-	+0.43

thereby stabilizing OH^- and O^{2-} ($\sim$ -0.90 e). The greatest difference between the surface and subsurface doping cases appears in the third step. At the surface V site, the nitrogen dopants revert to their N^{3-} oxidation state while a superoxide-like $O_2{}^-$ dimer forms (O–O = 1.32 Å, −0.58 e), driving the overpotential down to 0.93 V. In the subsurface model the nitrogen dopants also return to N^{3-}, but the reaction produces a peroxide-like $O_2{}^{2-}$ dimer (O–O = 1.44 Å, −0.95 e), leaving the overpotential at 1.60 V. These charge/bond-length assignments match the results reported by Österbacka *et al* [28] Complete charge data are given in the SI.

Next, we aim at a more detailed understanding of the origin of the lowered overpotentials when the reaction pathways involve a surface N site and a surface V atom. To this end, we calculate the adsorption energies of aqueous species, namely H^+, H_2O, and OH^- on different sites, to verify if a variation in the acid-base chemistry on the doped surface is the cause of the observed trends.

In addition to the acid-base reactions occurring on the pristine surface [48]:

$$H^+@O_{surf} \rightleftharpoons O_{surf} + H^+(aq)\,, \tag{22}$$

$$H_2O@Bi_{surf} \rightleftharpoons OH^-@Bi_{surf} + H^+(aq)\,. \tag{23}$$

The doped system also features the following reactions:

$$H^+@N_{surf} \rightleftharpoons N_{surf} + H^+(aq)\,, \tag{24}$$

$$H_2O@V_{surf} \rightleftharpoons OH^-@V_{surf} + H^+(aq)\,. \tag{25}$$

Therefore, we first compare (i) the adsorption energy of H^+ on the surface N with respect to that on a regular surface O site and (ii) the adsorption energies of H_2O and OH^- on a surface V atom against a Bi site. We hence define $\Delta_{ads}H^+$, $\Delta_{ads}H_2O$, $\Delta_{ads}OH^-$ as follows:

$$\Delta_{ads}H^+ = E\left[H^+@O_{surf}\right] - E\left[H^+@N_{surf}\right]\,, \tag{26}$$

$$\Delta_{ads}H_2O = E\left[H_2O@Bi_{surf}\right] - E\left[H_2O@V_{surf}\right]\,, \tag{27}$$

$$\Delta_{ads}OH^- = E\left[OH^-@Bi_{surf}\right] - E\left[OH^-@V_{surf}\right]\,. \tag{28}$$

This is simply the difference in hybrid DFT total-energy for the species adsorbed on different sites of the slab.

Results collected in table 1 indicate that proton adsorption is remarkably favored on the surface N site, as we calculate $\Delta_{ads}H^+ = 0.52$ eV, consistent with the results shown in figure 3. At variance with this, the energetics associated with the adsorption of a water molecule are quite similar for Bi and V site ($\Delta_{ads}H_2O = -0.08$ eV). However, the supercell bearing a surface hydroxyde anion is found to be more sizably stable when bound to a surface V atom ($\Delta_{ads}OH^- = 0.43$ eV). This indicates that dissociation of a water molecule is favored on surface V, thus contributing to the observed lowering of the overpotential for the first reaction steps. Moreover, the present analysis indicates that subsurface doping would not be beneficial, as the reaction sites would be essentially the same as those of the pristine bulk.

The calculated results allow for a quantitative estimate of the acidity for the N_{surf} and for $H_2O@V_{surf}$, in comparison with those of the sites available on the pristine surface (O_{surf} and $H_2O@Bi_{surf}$). Similarly to [33], we define the pK_a of N_{surf} and $H_2O@M_{surf}$ as relative to those of O_{surf} and $H_2O@Bi_{surf}$:

$$pK_a\left(N_{surf}\right) = pK_a\left(O_{surf}\right) + \frac{\Delta_{ads}H^+}{\ln 10 \cdot k_B T}\,, \tag{29}$$

$$pK_a\left(H_2O@V_{surf}\right) = pK_a\left(H_2O@Bi_{surf}\right) + \frac{\Delta_{ads}H_2O - \Delta_{ads}OH^-}{\ln 10 \cdot k_B T}\,, \tag{30}$$

Table 2. Calculated values (eV) of $\Delta_{dis}A[H_2O@M_{surf}]$ for M_{surf} = Bi, V with concurring H^+ adsorption on N or O. For the latter the values are given in parentheses.

M	$\Delta_{dis}A[H_2O@M_{surf}]$
Bi	$+0.19\ (+0.73)$
V	$-0.31\ (+0.05)$

i.e. the variation in acidic constants originates from the different adsorption energies of the aqueous species on N/O sites and Bi/V sites respectively. Since from a previous study [49], $pK_a(O_{surf}) = -1.88$ and $pK_a(H_2O@Bi) = 8.42$, we here achieve $pK_a(N_{surf}) = 5.60$ and $pK_a(H_2O@V) = 1.08$. Therefore, while the extremely acidic nature of surface O implied a negligible concentration of protons bound to the pristine $BiVO_4$ surface under a large range of operative pH conditions for photocatalytic systems, surface N-doping provides sites more readily available for binding H^+. Furthermore, surface V exhibiting a stronger interaction with the hydroxide anion also favor water dissociation, substantially increasing its acidity. We also note that the effects on the different sites are comparable in absolute value but in opposite direction, i.e. N_{surf} is more alkaline than O_{surf} while $H_2O@V_{surf}$ is more acidic than $H_2O@Bi_{surf}$. Therefore, the effect on the pH of zero charge of the material, i.e the value of pH at which the surface is electrically neutral, is likely to not be particularly varied. However, the concentration of adsorbed ionic species (H^+ and OH^-) will indeed be different. In fact, we define the dissociation of a water molecule adsorbed on a metal site M as:

$$H_2O@M_{surf} \rightleftharpoons OH^-@M_{surf} + H^+@X_{surf}, \tag{31}$$

where M_{surf} = Bi, V and X_{surf} = N, O, whose free-energy reads as [48]:

$$\Delta_{dis}A\left[H_2O@M_{surf}\right] = \ln 10 \cdot k_B T\left[pK_a\left(H_2O@Bi_{surf}\right) - pK_a\left(X_{surf}\right)\right]. \tag{32}$$

In table 2, we report the calculated values of $\Delta_{dis}A[H_2O@M_{surf}]$ for water molecules adsorbed on Bi and V, with concurring H^+ adsorption either on N or O. Both surface N and V contribute to making water dissociation more favorable with respect to the pristine material. In particular, when the dissociation occurs only on these sites, the reaction becomes exergonic.

Overall, surface N-doping appears to have remarkable beneficial effects on the acid-base surface chemistry of $BiVO_4$ (001) surface, which is key in lowering overpotentials, and consequently, contributing to the better performance observed for the doped system.

In addition to the AEM mechanism, we also examined the DSBM mechanism. The most stable OER intermediates (*OH and *O) [reactions (10)–(13)] for the N-$BiVO_4$ surface doping and subsurface doping cases are illustrated in figure 7, with their corresponding free energy profiles (equations (14)–(17)) shown in figure 8. Under the DSBM mechanism, surface doping results in a substantially lower η of 1.16 V compared to both pristine $BiVO_4$ (1.44 V) and subsurface doping (1.92 V). A closer examination of the individual reaction steps, from deprotonation of *OH–*OH to the formation of *O–*OH, demonstrates that surface doping benefits from a more favorable free-energy pathway, highlighting the enhanced catalytic efficiency enabled by surface nitrogen doping. In contrast, the steeper energy gradient on the subsurface doping results in a higher η of 1.92 V, indicating that nitrogen doping at the subsurface is less advantageous for OER catalysis.

Although the dual-site DSBM (η = 1.16 V) is less efficient than the single-site AEM pathway (η = 0.93 V), both mechanisms feature overpotentials lower by $\geqslant$0.3 V relative to pristine $BiVO_4$ (η = 1.44 V), demonstrating that N-$BiVO_4$ enhances OER activity irrespective of whether the reaction proceeds at a single V site or cooperatively across a Bi–V pair. The AEM pathway is favorable with lower overpotential, however, if the surface is defect-rich, the *O–*O coupling route could become viable [50]. Previous research showed that at pH > 8.2 the $BiVO_4$(010) surface becomes hydroxylated, providing the *OH reservoir that deprotonates to *O as potential increase [49]. Under anodic bias and light, operando spectra reveal a strongly oxidizing, dynamically reconstructed interface, consistent with deeper deprotonation from *OH to *O [51]. Defects that place oxo sites next to each other further stabilize *O and enable direct *O–*O coupling, bypassing the *OOH penalty that limits AEM [50]. Thus, the DSBM can happen in extreme or engineered conditions that populate dual oxygen sites, thereby opening a more efficient pathway for O_2 evolution. Overall, these results highlight the role of surface doping strategies in governing OER performance and offer valuable guidance for the development of more efficient $BiVO_4$-based photoanodes.

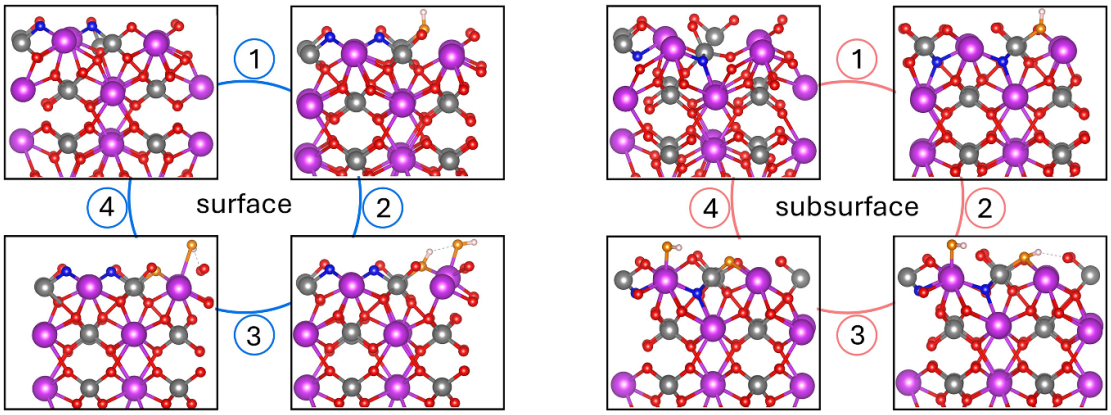

Figure 7. Side view of the DSBM reaction cycle, equations (10)–(13), for N-$BiVO_4$ surface and subsurface doping.

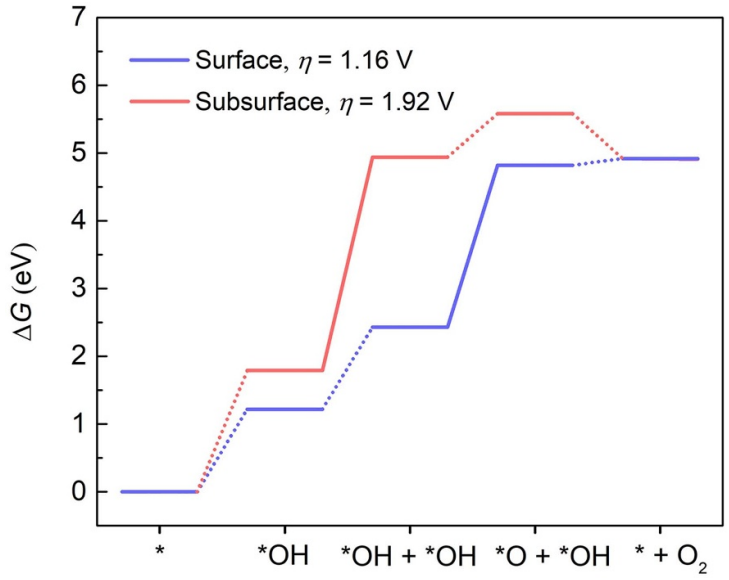

Figure 8. Free energy profiles of N-$BiVO_4$ surface and subsurface with DSBM mechanism.

4. Conclusions

In summary, we employed hybrid DFT calculations to investigate how nitrogen doping and oxygen vacancy formation synergistically enhanced the OER performance of $BiVO_4$. By substituting two surface oxygen atoms with nitrogen and introducing an oxygen vacancy for charge neutrality, we evaluated the catalytic activity at both the surface doping and subsurface doping under two distinct OER pathways: the AEM and the DSBM.

Our results show that nitrogen doping on the surface, which creates a V-based active site, substantially boosts OER activity. Under the AEM pathway, the OER η decreases from 1.44 V in pristine $BiVO_4$ to 1.28 V at the surface Bi site, and further to 0.93 V at the V site. In contrast, subsurface doping yields only a modest benefit at the Bi site (η = 1.42 V) and even worsens performance at the V site (η = 1.60 V). Charge-state analysis shows that the extra electron from nitrogen donation to $^*OH^-$ explains the modest overpotential drop at Bi sites. At the V site, surface doping stabilizes a superoxide-like O_2^{1-} dimer (O–O = 1.32 Å, −0.58 e), whereas subsurface doping favors a peroxide-like O_2^{2-} species (O-O = 1.44 Å, −0.95 e). Additionally, we find that nitrogen dopants profoundly change the local acid–base equilibria. Proton adsorption is 0.52 eV more favorable at the N site than on the O site, and water dissociation is 0.43 eV more favorable at a V site than at Bi site. The nitrogen dopants stabilize $^*OH^-$, $^*O^-$, as well as the superoxide-like O_2^{1-} dimer, and facilitate proton adsorption, resulting in the lower overpotential. Under the DSBM pathway, η is reduced to 1.16 V for the surface doping case and increased to 1.92 eV at subsurface doping. Therefore, nitrogen doping at the surface plays a direct and active role in

enhancing OER performance. In contrast, nitrogen doping at the subsurface offers minimal benefits, or worsens performance, regardless of whether the AEM or DSBM pathway is followed, underscoring the importance of doping site selection. Although the absolute overpotentials remain above those of benchmark OER catalysts, the $\geqslant$0.3 eV drop we observe demonstrates that N-doping and oxygen vacancies create a more active $BiVO_4$-based photoanode surface that can synergize with photovoltage and standard co-catalyst overlayers in practical PEC devices.

Supporting information

All nitrogen doped $BiVO_4$ surface and subsurface configurations are described here. Figures S1 and S2 present a comparison of the energy difference between nitrogen-doped $BiVO_4$ surface and subsurface with oxygen vacancy introduced at various sites. Figure S3 show the $BiVO_4$ surface and subsurface configurations after AIMD simulation. Table S1 summarizes the defect formation energies of N-$BiVO_4$ surface and subsurface. Table S2 summarizes DDEC6 net atomic charges for the two nitrogen dopants (N1, N2) and for every adsorbed intermediate.

Notes

The authors declare no competing financial interest.

Data availability statement

All data that support the findings of this study are included within the article (and any supplementary files).

Supplementary data 1 available at https://doi.org/10.1088/2515-7655/ae1061/data1.

Acknowledgments

We acknowledge funding from the Swedish Strategic Research Foundation through a Future Research Leader programme (FFL21-0129), the Swedish Energy Agency (Grant No. 45410-1), the Swedish Research Council (2018-06482, 2019-03993, and 2020-04935), the Knut and Alice Wallenberg Foundation (Nos. 2023.0032 and 2024.0042), and the Area of Advance Energy at Chalmers is gratefully acknowledged. The computations were enabled by resources provided by the National Academic Infrastructure for Supercomputing in Sweden (NAISS) at C3SE, PDC, and NSC, partially funded by the Swedish Research Council through grant agreement no. 2022-06725. Funded by the European Union (ERC, POLARISE, 101162195). Views and opinions expressed are however those of the authors only and do not necessarily reflect those of the European Union or the European Research Council. Neither the European Union nor the granting authority can be held responsible for them. F A thankfully acknowledge PRIN 2022-PNRR grant (P2022W9773) for funding and the CINECA award under the ISCRA initiative, for the availability of high-performance computing resources: projects MHP-DEF and Photofix.

ORCID iDs

Qiuhua Liang 0000-0002-5436-5203
Hassan Ouhbi 0000-0001-7371-4782
Nicklas Österbacka 0000-0002-6043-4607
Francesco Ambrosio 0000-0002-6388-9586
Julia Wiktor 0000-0003-3395-1104

References

[1] Maeda K, Teramura K, Lu D, Takata T, Saito N, Inoue Y and Domen K 2006 Photocatalyst releasing hydrogen from water *Nature* **440** 295
[2] Walter M G, Warren E L, McKone J R, Boettcher S W, Mi Q, Santori E A and Lewis N S 2010 Solar water splitting cells *Chem. Rev.* **110** 6446–73
[3] Yang W, Prabhakar R R, Tan J, Tilley S D and Moon J 2019 Strategies for enhancing the photocurrent, photovoltage and stability of photoelectrodes for photoelectrochemical water splitting *Chem. Soc. Rev.* **48** 4979–5015
[4] Fabbri E, Habereder A, Waltar K, Kötz R and Schmidt T J 2014 Developments and perspectives of oxide-based catalysts for the oxygen evolution reaction *Catal. Sci. Technol.* **4** 3800–21
[5] Zhang X and Bieberle-Hütter A 2016 Modeling and simulations in photoelectrochemical water oxidation: from single level to multiscale modeling *ChemSusChem* **9** 1223–42

[6] Liang Q, Brocks G, Sinha V and Bieberle-Hütter A 2021 Tailoring the performance of ZnO for oxygen evolution by effective transition metal doping *ChemSusChem* **14** 3064–73
[7] Djurišić A B, Leung Y H and Ng A M C 2014 Strategies for improving the efficiency of semiconductor metal oxide photocatalysis *Mater. Horiz.* **1** 400–10
[8] Antipin D and Risch M 2020 Trends of epitaxial perovskite oxide films catalyzing the oxygen evolution reaction in alkaline media *J. Phys. Energy* **2** 032003
[9] Park Y, McDonald K J and Choi K S 2013 Progress in bismuth vanadate photoanodes for use in solar water oxidation *Chem. Soc. Rev.* **42** 2321–37
[10] Kim T W and Choi K S 2014 Nanoporous $BiVO^4$ photoanodes with dual-layer oxygen evolution catalysts for solar water splitting *Science* **343** 990–4
[11] Wiktor J, Ambrosio F and Pasquarello A 2018 Role of polarons in water splitting: the case of $BiVO_4$ *ACS Energy Lett.* **3** 1693–7
[12] Abdi F F, Savenije T J, May M M, Dam B and Van De Krol R 2013 The origin of slow carrier transport in $BiVO^4$ thin film photoanodes: a time-resolved microwave conductivity study *J. Phys. Chem. Lett.* **4** 2752–7
[13] Gahlawat S, Schnell P, Irani R, Ahmet I Y, Choubrac L, Fiechter S, Ingole P P and Abdi F F 2022 Extending the absorption limit of $BiVO^4$ photoanodes with hydrogen sulfide treatment *Sol. RRL* **6** 2200129
[14] Quinonero J, Lana-Villarreal T and Gómez R 2016 Improving the photoactivity of bismuth vanadate thin film photoanodes through doping and surface modification strategies *Appl. Catal. B* **194** 141–9
[15] Jeong H W, Jeon T H, Jang J S, Choi W and Park H 2013 Strategic modification of $BiVO^4$ for improving photoelectrochemical water oxidation performance *J. Phys. Chem. C* **117** 9104–12
[16] Jeong S Y *et al* 2017 Enhanced photocatalytic performance depending on morphology of bismuth vanadate thin film synthesized by pulsed laser deposition *ACS Appl. Mater. Interfaces* **9** 505–12
[17] Lin X, Yu L, Yan L, Li H, Yan Y, Liu C and Zhai H 2014 Visible light photocatalytic activity of $BiVO^4$ particles with different morphologies *Solid State Sci.* **32** 61–66
[18] Vishlaghi M B, Kahraman A, Österbacka N, Usman E, Erdem E, Sennaroğlu A, Wiktor J and Kaya S 2023 Accelerating water oxidation on $BiVO^4$ photoanodes via surface modification with Co dopants *J. Mater. Chem. A* **11** 16648–58
[19] Rettie A J E, Lee H C, Marshall L G, Lin J F, Capan C, Lindemuth J, McCloy J S, Zhou J, Bard A J and Mullins C B 2013 Combined charge carrier transport and photoelectrochemical characterization of $BiVO^4$ single crystals: intrinsic behavior of a complex metal oxide *J. Am. Chem. Soc.* **135** 11389–96
[20] Park H S, Kweon K E, Ye H, Paek E, Hwang G S and Bard A J 2011 Factors in the metal doping of $BiVO^4$ for improved photoelectrocatalytic activity as studied by scanning electrochemical microscopy and first-principles density-functional calculation *J. Phys. Chem. C* **115** 17870–9
[21] Hu J, Zhao X, Chen W, Su H and Chen Z 2017 Theoretical insight into the mechanism of photoelectrochemical oxygen evolution reaction on $BiVO^4$ anode with oxygen vacancy *J. Phys. Chem. C* **121** 18702–9
[22] Wang W, Strohbeen P J, Lee D, Zhou C, Kawasaki J K, Choi K S, Liu M and Galli G 2020 The role of surface oxygen vacancies in $BiVO^4$ *Chem. Mater.* **32** 2899–909
[23] Wang G, Ling Y, Lu X, Qian F, Tong Y, Zhang J Z, Lordi V, Rocha Leao C and Li Y 2013 Computational and photoelectrochemical study of hydrogenated bismuth vanadate *J. Phys. Chem. C* **117** 10957–64
[24] Su J, Guo L, Bao N and Grimes C A 2011 Nanostructured $WO_3/BiVO^4$ heterojunction films for efficient photoelectrochemical water splitting *Nano Lett.* **11** 1928–33
[25] Hong S J, Lee S, Jang J S and Lee J S 2011 Heterojunction $BiVO^4/WO_3$ electrodes for enhanced photoactivity of water oxidation *Energy Environ. Sci.* **4** 1781–7
[26] Chang X, Wang T, Zhang P, Zhang J, Li A and Gong J 2015 Enhanced surface reaction kinetics and charge separation of p–n heterojunction $Co_3O_4/BiVO_4$ photoanodes *J. Am. Chem. Soc.* **37** 8356–9
[27] Seo H, Ping Y and Galli G 2018 Role of point defects in enhancing the conductivity of $BiVO^4$ *Chem. Mater.* **30** 7793–802
[28] Österbacka N, Ouhbi H, Ambrosio F and Wiktor J 2023 Spontaneous oxygen vacancy ionization enhances water oxidation on $BiVO^4$ *ACS Energy Lett.* **9** 153–8
[29] Kim T W, Ping Y, Galli G A and Choi K S 2015 Simultaneous enhancements in photon absorption and charge transport of bismuth vanadate photoanodes for solar water splitting *Nat. Commun.* **6** 8769
[30] Kühne T D *et al* 2020 CP2K: an electronic structure and molecular dynamics software package–quickstep: efficient and accurate electronic structure calculations *J. Chem. Phys.* **152** 194103
[31] Goedecker S, Teter M and Hutter J 1996 Separable dual-space Gaussian pseudopotentials *Phys. Rev. B* **54** 1703
[32] VandeVondele J and Hutter J 2007 Gaussian basis sets for accurate calculations on molecular systems in gas and condensed phases *J. Chem. Phys.* **127** 114105
[33] Ambrosio F and Wiktor J 2019 Strong hole trapping due to oxygen dimers in $BiVO^4$: effect on the water oxidation reaction *J. Phys. Chem. Lett.* **10** 7113–8
[34] Wiktor J, Reshetnyak I, Ambrosio F and Pasquarello A 2017 Comprehensive modeling of the band gap and absorption spectrum of $BiVO^4$ *Phys. Rev. Mater.* **1** 022401
[35] Kudo A, Omori K and Kato H 1999 A novel aqueous process for preparation of crystal form-controlled and highly crystalline $BiVO^4$ powder from layered vanadates at room temperature and its photocatalytic and photophysical properties *J. Am. Chem. Soc.* **121** 11459–67
[36] Rossmeisl J, Qu Z W, Zhu H, Kroes G J and Nørskov J K 2007 Electrolysis of water on oxide surfaces *J. Electroanal. Chem.* **607** 83–89
[37] Liang Q, Brocks G and Bieberle-Hütter A 2021 Oxygen evolution reaction (OER) mechanism under alkaline and acidic conditions *J. Phys. Energy* **3** 026001
[38] Cao H, Wen X, Luo X, Ma L, Xu Z, Zhang Z and Zhang W 2024 Dual-site bridging mechanism for bimetallic electrochemical oxygen evolution *Angew. Chem.* **136** e202411683
[39] Barlocco I, Cipriano L A, Di Liberto G and Pacchioni G 2023 Does the oxygen evolution reaction follow the classical OH*, O*, OOH^* path on single atom catalysts? *J. Catal.* **417** 351–9
[40] Qin Q, Li Z, Zhao X, Zhao H, Zhai L, Gyu Kim M, Cho J, Jang H, Liu S and Liu X 2025 Atomically dispersed vanadium-induced Ru-V dual active sites enable exceptional performance for acidic water oxidation *Angew. Chem.* **137** e202413657
[41] Nørskov J K, Rossmeisl J, Logadottir A, Lindqvist L R K J, Kitchin J R, Bligaard T and Jonsson H 2004 Origin of the overpotential for oxygen reduction at a fuel-cell cathode *J. Phys. Chem. B* **108** 17886–92

[42] Sokolov M, Doblhoff-Dier K and Exner K S 2024 Best practices of modeling complex materials in electrocatalysis, exemplified by oxygen evolution reaction on pentlandites *Phys. Chem. Chem. Phys.* **26** 22359–70
[43] Romeo E, Illas F and Calle-Vallejo F 2023 Evaluating adsorbate–solvent interactions: are dispersion corrections necessary? *J. Phys. Chem. C* **127** 10134–9
[44] Tillotson M J, Brett P M, Bennett R A and Grau-Crespo R 2015 Adsorption of organic molecules at the tio2 (110) surface: the effect of van der Waals interactions *Surf. Sci.* **632** 142–53
[45] Österbacka N, Ambrosio F and Wiktor J 2022 Charge localization in defective $BiVO^4$ *J. Phys. Chem. C* **126** 2960–70
[46] Manz T A and Limas N G 2016 Introducing DDEC6 atomic population analysis: part 1. charge partitioning theory and methodology *RSC Adv.* **6** 47771–801
[47] Liang Q, Bieberle-Hütter A and Brocks G 2022 Anti-ferromagnetic RuO_2: a stable and robust oer catalyst over a large range of surface terminations *J. Phys. Chem. C* **126** 1337–45
[48] Ambrosio F, Wiktor J and Pasquarello A 2018 pH-dependent catalytic reaction pathway for water plitting at the $BiVO^4$–water interface from the band alignment *ACS Energy Lett.* **3** 829–34
[49] Ambrosio F, Wiktor J and Pasquarello A 2018 pH-dependent surface chemistry from first principles: application to the $BiVO^4$(010)–water interface *ACS Appl. Mater. Interfaces* **10** 10011–21
[50] Nikacevic P, Hegner F S, Galán-Mascarós J R and Lopez N 2021 Influence of oxygen vacancies and surface facets on water oxidation selectivity toward oxygen or hydrogen peroxide with bivo4 *ACS Catal.* **11** 13416–22
[51] Venugopal A, Kas R, Hau K and Smith W A 2021 Operando infrared spectroscopy reveals the dynamic nature of semiconductor–electrolyte interface in multinary metal oxide photoelectrodes *J. Am. Chem. Soc.* **143** 18581–91